Single-Particle Characterization of Aβ Oligomers in Solution

Erik C. Yusko,[†] Panchika Prangkio,[†] David Sept,[†,‡] Ryan C. Rollings,[§] Jiali Li,[§] and Michael Mayer[†,⊥,*]

[†]Department of Biomedical Engineering, University of Michigan, Ann Arbor, Michigan 48109, United States, [‡]Center for Computational Medicine and Biology, University of Michigan, Ann Arbor, Michigan 48109, United States, [§]Department of Physics, University of Arkansas, Fayetteville, Arkansas, 72701, United States, and [⊥]Department of Chemical Engineering, University of Michigan, Ann Arbor, Michigan 48109, United States

ABSTRACT Determining the pathological role of amyloids in amyloid-associated diseases will require a method for characterizing the dynamic distributions in size and shape of amyloid oligomers with high resolution. Here, we explored the potential of resistive-pulse sensing through lipid bilayer-coated nanopores to measure the size of individual amyloid-β oligomers directly in solution and without chemical modification. This method classified individual amyloid-β aggregates as spherical oligomers, protofibrils, or mature fibers and made it possible to account for the large heterogeneity of amyloid-β aggregate sizes. The approach revealed the distribution of protofibrillar lengths (12- to 155 -mer) as well as the average cross-sectional area of protofibrils and fibers.

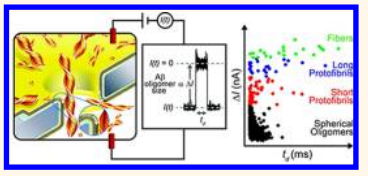

KEYWORDS: nanopore · single molecule · bilayer-coated nanopore · amyloid-beta oligomer · amyloid aggregate · amyloid fiber · protofibril · resistive pulse · cluster analysis · Coulter counter · size distribution · bootstrap resampling · cumulative distribution function · probability density function

Aberrant aggregation of amyloidogenic proteins and peptides is associated with the pathophysiology of several diseases including Alzheimer's disease, Parkinson's disease, Huntington's disease, and type II diabetes mellitus.[1−5] Although these amyloid aggregates are associated with many cytotoxic effects,[1] their toxic form and pathogenic mechanisms remain generally unclear.[6,7] One reason for the lack in understanding is that the size and shape of amyloid oligomers are typically heterogeneous and dynamic in solution.[8] Consequently, the potential toxic effects of subpopulations of oligomers in these heterogeneous preparations are difficult to discern as these subpopulations are often masked in ensemble measurement techniques.[8,9] For example, Cabriolu *et al.* recently developed a computational model describing the size distribution of aggregates of amyloid-β, the peptide implicated with Alzheimer's disease,[10] and reported the occurrence of "magic" fibril sizes: preferred aggregate sizes that appear as peaks in the distribution.[11,12] The authors could only qualitatively verify this result[13] because of a "lack of suitable experimental or simulation data for the size distribution of amyloid fibrils".[11] Here, we make a first attempt to determine the size and shape distributions of unlabeled Aβ aggregates in solution by analyzing resistive current pulses from hundreds of single aggregates during their passage through an electrolyte-filled nanopore. We propose that resistive pulse sensing is an enabling technique for characterizing aggregated amyloidogenic peptides, since it is the only technique that measures single particles volumetrically and is, therefore, particularly well-suited for characterizing particles with irregular shapes.[14]

Increasing evidence indicates that certain sizes of Aβ oligomers, and possibly certain shapes of these oligomers, are more neurotoxic than others and, thus, play different roles in the pathology of Alzheimer's disease.[10,15−21] Aggregated forms of Aβ in the brain are thought to stem from an imbalance between the generation and clearance of Aβ monomers, which subsequently leads to their accumulation and aggregation[6,22] to oligomers,[15] protofibrils,[17,23] fibers,[18] and amyloid plaques.[6] The sizes of Aβ oligomers range from the monomer molecular weight of 4.3 kDa for the 40 amino acid peptide to ∼43 kDa,[24] whereas protofibrils have molecular weights greater than ∼43 kDa and are approximately 5 nm in diameter and less than ∼200 nm in length.[24,25] Fibers result from the assembly of protofibrils and have an average diameter of approximately 7−10 nm and lengths up to several micrometers,[25−27] while senile plaques are dense meshes of Aβ fibers in the brain.[6,7]

One reason that the pathogenic role of different Aβ aggregates in Alzheimer's disease is not understood stems from conflicting reports and difficulties reproducing the exact conditions of previous experiments.[6,7,21,28] Conducting assays with reproducible distributions of Aβ aggregates is challenging, since

* Address correspondence to mimayer@umich.edu.

Received for review February 6, 2012 and accepted June 11, 2012.

Published online June 11, 2012
10.1021/nn300542q

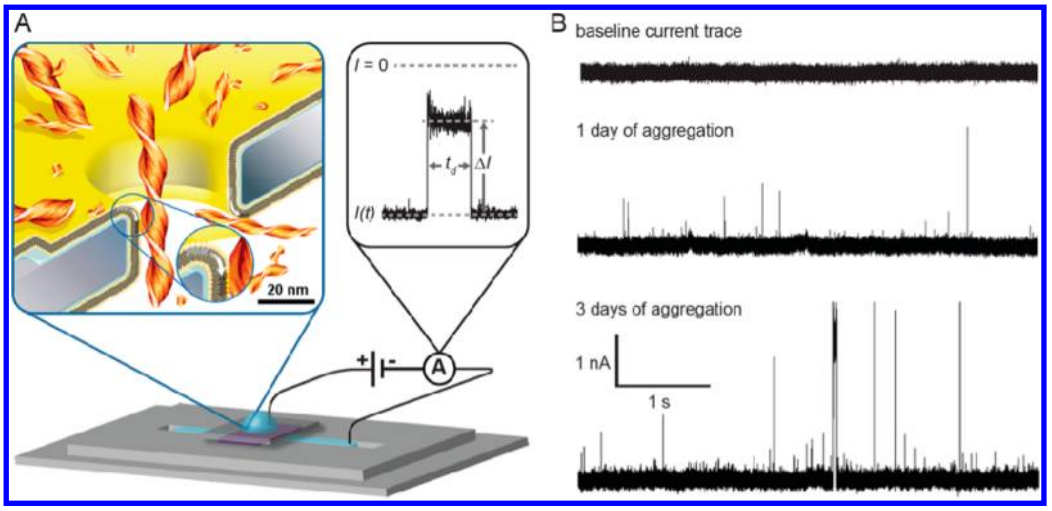

Figure 1. Synthetic nanopores with fluid walls make it possible to characterize individual Aβ aggregates by resistive-pulse recordings. (A) Illustration of the experimental setup with fluid access channels to a nanopore embedded in a silicon nitride chip.[58,59] Silver−silver/chloride electrodes immersed in the two fluidic compartments are connected to a patch-clamp amplifier and used to measure the ionic current through the nanopore. Inset left: Cartoon showing a cross-section of a nanopore that is coated with a fluid lipid bilayer, thereby enabling the translocation of Aβ aggregates without clogging the pore. Inset right: Original current trace showing a characteristic resistive pulse with the parameters ΔI and t_d. (B) Original current traces recorded before and after adding Aβ that was permitted to aggregate for 1 or 3 days. The nanopore had a length of 18 nm and a diameter of 28 nm before the lipid bilayer coating (length of 28 nm and a diameter of 18 nm after the bilayer coating).

temperature, concentration, pH, solvent conditions, solvent history, agitation, and air−water interfaces strongly influence nucleation and aggregation rates and the distribution of aggregate shapes and sizes.[24] Consequently, methods for characterizing the distribution of aggregated species quickly, accurately, and in solution are needed to interpret functional studies as well as to determine the pathological role of amyloidogenic peptides in Alzheimer's disease and other neurodegenerative disorders.[10,24,29]

Several techniques are currently being used to characterize the aggregation and structure of Aβ aggregates. Gel electrophoresis with native gels and SDS gels makes it possible to identify and separate low molecular weight Aβ aggregates; however, the technique can misrepresent the native aggregation state and can accurately resolve only low-molecular weight aggregates (*i.e.*, less than decamers).[24,29] Size exclusion chromatography is considered the best non-SDS-based method for identifying and separating Aβ aggregates, although, it is a relatively low resolution method compared to SDS-PAGE.[8,29] Electron microscopy and atomic force microscopy imaging techniques provide the highest quality information on the structure of Aβ aggregates; however, they require drying the sample and the results may be affected by biased adsorption of the aggregates to the TEM substrates.[26,27,30,31] Light-scattering techniques permit *in situ* measurements, but they are ill-suited for monitoring fibrillar objects and heterogeneous populations such as those found in solutions containing Aβ aggregates.[24,32] Circular dichroism,[23,24] thioflavin T fluorescence assays,[13] and surface-enhanced Raman spectroscopy[33] monitor changes in the conformation of Aβ during aggregation but do not provide information on the size of aggregates.[29]

Recently, the first attempts to apply single-molecule techniques toward Aβ aggregation and toxicology studies emerged. Knowles *et al*. combined the thioflavin T assay with a microfluidic technique to follow amyloid aggregation from single-aggregate nuclei.[34] Schierle *et al*. used a super-resolution fluorescence imaging technique to image, *in situ* and in live cells, individual aggregates of Aβ with sizes greater than ~20 nm.[35] The technique requires covalent modification of Aβ monomers with a fluorophore or the binding of fluorescently labeled antibodies to Aβ aggregates. Wang *et al*. used the resistive-pulse sensing technique with the biological α-hemolysin pore to assess conformational changes in $A\beta_{(1-42)}$ aggregates that were induced by Congo red or β-cyclodextrin (two molecules with opposite effects on $A\beta_{(1-42)}$ aggregation).[36] Finally, Dukes *et al*., Schauerte *et al*., Ding *et al*., and Johnson *et al*. used fluorescently labeled Aβ peptides combined with single-molecule fluorescence spectroscopy to measure the aggregation of single $A\beta_{(1-40)}$ peptides and the binding of single aggregates to model membranes and cell membranes.[8,9,37,38] These techniques exemplify the search for single-molecule techniques capable of detecting individual aggregates of Aβ *in situ* in order to determine the heterogeneous size distribution of aggregates, their kinetics of assembly, and their pathogenic function.[10]

With the same goal in mind, we recently demonstrated that lipid-coated, electrolyte-filled nanopores in a resistive-pulse sensing configuration could be

used to detect Aβ fibers in solution without drying, chemically modifying, or labeling Aβ samples.[39] Resistive-pulse sensing[40−52] is an attractive technique to characterize heterogeneous samples since the magnitudes of transient changes in ionic current, ΔI, are due to the translocation of individual particles through the nanopore (Figure 1A) and are proportional to the volume of electrolyte excluded by the aggregate.[39,53,54] Additionally, the duration of the resistive pulse, t_d, is related to the electrophoretic mobility of the aggregate, and the frequency of translocation events is related to the concentration of the particles.[39,55−57]

Here, we extend the use of lipid-coated, synthetic nanopores from analyzing Aβ fibers to characterizing the smaller and clinically more relevant soluble Aβ oligomers. The lipid coating of the nanopore (Figure 1A inset) is required for detection of Aβ aggregates, since synthetic nanopores without a fluid coating clogged due to adsorption of Aβ on the nanopore walls (see Supporting Information Figure S1).[39] We show that resistive-pulse sensing with lipid-coated nanopores can be used to track the time-dependent aggregation of $A\beta_{(1-40)}$ by monitoring the size distribution of Aβ aggregates in solution, and we validated this method by analyzing transmission electron microscopy micrographs of $A\beta_{(1-40)}$ aggregates from the same Aβ preparations.

RESULTS AND DISCUSSION

To perform nanopore-based detection of $A\beta_{(1-40)}$ aggregates, we started from aqueous solutions containing mostly monomers of $A\beta_{(1-40)}$ as well as dimeric and trimeric aggregates that are thought to be in rapid equilibrium with the monomeric form[24] (Supporting Information S2). We prepared aggregates of $A\beta_{(1-40)}$ by incubating these solutions for zero to three days under well-controlled conditions before adding 1−2.5 μL of these Aβ preparations to the electrolyte in the top compartment of the recording setup (Figure 1A).[24,60] Gel electrophoresis confirmed that this preparation method resulted in increasing aggregate sizes over time (Supporting Information S2).[60] Additionally, circular dichroism spectroscopy and thioflavin T binding assays showed an increase in β-sheet content and fibril formation with increasing aggregation time (Supporting Information S3). Cytotoxicity assays confirmed that this preparation method resulted in aggregates that were biologically active and yielded similar toxicity characteristics to those reported in the literature (Supporting Information S3).[10,61,62]

Figure 1B shows recordings of the baseline current before and after adding $A\beta_{(1-40)}$ solutions that had been permitted to aggregate for one or three days. Consistent with time-dependent aggregation, the current trace from the three-day sample shows resistive pulses with increased frequency and larger amplitude than the current trace from the one-day sample. Figure 2A shows scatter plots of ΔI *versus* t_d values for translocation events with a ΔI value greater than 250 pA (5 times the standard deviation of the noise) and with a t_d value greater than 35 μs (the smallest t_d value we could measure accurately).[39,63] As expected, the values of ΔI, and hence the sizes of aggregates, increased with increasing aggregation time. Interestingly, the amplitude of ΔI values reached a maximum at ∼5 nA, which was only 19% of the 26 nA baseline current magnitude, despite large variations in t_d values (Figure 2B, cluster (iv)). This result is consistent with translocation of cylindrical objects with similar diameters but varying lengths that are longer than the length of the nanopore, similar to the translocation of DNA strands of varying lengths.[59,64−67] Protofibrils, which have lengths up to 200 nm, and fibers, which can reach lengths of several micrometers, have these characteristics: both types of aggregates have nearly constant average diameters along their widely varying lengths,[12,25−27] and therefore, resistive pulses due to their translocation will have a maximum ΔI value and broadly distributed t_d values.[12,25]

In order to distinguish among resistive pulses resulting from the translocation of spherical oligomers, protofibrils, or fibers through the nanopore, we performed a cluster analysis on a data set from all resistive pulses (Figure 2B) based on the ΔI value for each translocation event. To perform the cluster analysis, we used the *k-means* algorithm in the open-source, statistics software R (http://www.R-project.org) and set the number of clusters to four, since we expected four clusters of ΔI *versus* t_d values that represented the translocation of (i) spherical oligomers, (ii) cylindrical protofibrils with lengths shorter than the effective length of the nanopore, (iii) cylindrical protofibrils with lengths longer than the effective length of the nanopore, or (iv) fibers with a length longer than the effective length of the nanopore. The open and filled symbols in Figure 2B illustrate the resulting cluster assignment given to each recorded resistive pulse. To test the robustness of this clustering procedure, we performed bootstrap resampling combined with *k-means* clustering to track the stability of the cluster classification for each point.[69] This analysis revealed that 82% of the measured ΔI values were classified into the same clusters at least 90% of the time. These points are indicated by filled-colored symbols in Figure 2B (Supporting Information S4).

Figure 2B reveals that cluster (iv) contains resistive pulses with very long transit times (up to 200 ms) and ΔI values that converge to a maximum value of 4 to 5 nA. This result would be expected for fibrils of varying lengths but relatively constant diameters. Cluster (iii) also contains pulses with long transit times (up to 60 ms) whose median is three times larger than the median transit time in cluster (ii). In both clusters

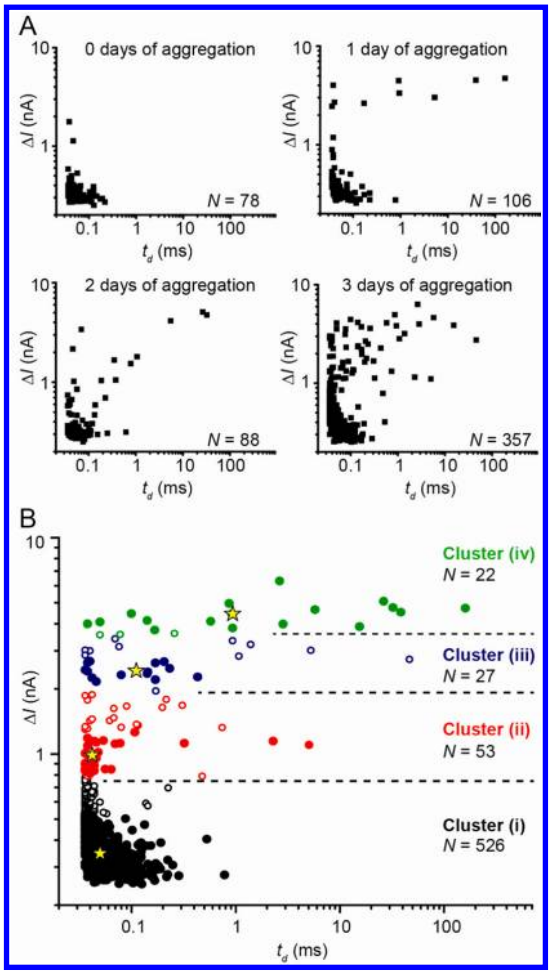

Figure 2. Scatter plots of ΔI values *versus* t_d values from the translocation of individual Aβ aggregates reveal clusters of translocation events due to spherical oligomers, protofibrils with lengths shorter than the length of the nanopore, protofibrils with lengths longer than the length of the nanopore, and mature fibers. (A) Scatter plots of $\Delta I(t_d)$ from aggregates of A$\beta_{(1-40)}$ that were analyzed after 0, 1, 2, and 3 days of incubation. (B) Scatter plot of all data combined and color coded according to the results from statistical cluster analysis.[68] Open and filled symbols show the results of the cluster classification based on the original data set. Filled symbols indicate points that were classified in the same cluster in more than 90% bootstrap resamples (Supporting Information S4). Yellow stars indicate the mean ΔI value and median t_d value based on the filled symbols in each cluster.

(iii) and (iv), the range of t_d values is greatly distributed over 2 to 4 orders of magnitude and toward longer translocation times than those observed in cluster (i) or (ii). Broad distributions of t_d values over a full order of magnitude can be expected due to the stochastic nature of molecular diffusion combined with biased motion by electrophoresis.[67,70] Additional effects such as nonspecific interactions between analytes and the pore walls with various frequencies and strengths can further increase the width of distributions of t_d such that they range several orders of magnitude even for the exact same analyte.[45,48] In the work presented here, the broadly distributed lengths of aggregates have an additional effect on t_d values; for instance protofibrils can have lengths ranging from ~10 to 200 nm, and fibers can have lengths ranging from less than one micrometer to several micrometers. The combination of large variations in length, stochastic elements of transit times through the pore, and potential for nonspecific binding results in large variations in t_d values. Despite these effects, several groups showed that median t_d values of molecules that are longer than the length of the pore increase with aggregate length.[59,64−66] Indeed, the yellow stars in Figure 2B show that median t_d values increased from cluster (ii) to cluster (iii) and cluster (iv), indicating the expected result that cluster (iv) contains longer aggregates than cluster (iii), which in turn contains longer aggregates than cluster (ii). This result, the broadly distributed t_d values in clusters (iii) and (iv), and the convergent maximal ΔI values in cluster (iv) suggest that the resistive pulses in these two clusters originated from the translocation of protofibrils and fibers with various lengths and nearly constant diameters.

To determine the size of A$\beta_{(1-40)}$ aggregates in each cluster, we used the value of ΔI from each translocation event and considered two extreme cases yielding two different equations.[39,53,70] Equation 1 describes the relationship between ΔI and the excluded volume, Λ (nm^3), of spherical oligomers,[71−74] whereas eq 2 describes the relationship between ΔI and the average cross-sectional area, A_X (nm^2), of aggregates with lengths longer than the effective length of the nanopore.[67,70]

$$\Delta I = \frac{\gamma V_A \Lambda}{\rho(l_P + 1.6 r_P)^2} \text{ for } l_M < l_{eff} \quad (1)$$

$$\Delta I = \frac{\gamma V_A A_X}{\rho(l_P + 1.6 r_P)} \text{ for } l_M > l_{eff} \quad (2)$$

In these equations, γ is a shape factor (with a value of 1.5 for globular spheres and a value of 1.0 for long cylinders that are aligned parallel to the electric field),[53,54,75−78] V_A (V) is the applied electric potential difference, ρ (Ω m) is the resistivity of the electrolyte solution, l_P (m) is the length of the nanopore, r_P (m) is the radius of the nanopore, and l_M (m) is the length of the protofibril or fiber. The effective length of the cylindrical nanopore, l_{eff}, is defined by the term (l_P + 1.6r_P) in the denominator of eqs 1 and 2, and it accounts for the extension of the electric field lines from the nanopore into the bulk solution.[79]

Table 1 lists the mean value of ΔI and the range of ΔI values that we measured for each cluster as well as the values for the excluded volume that we calculated using eq 1 for cluster (i) and the values for the cross-sectional areas that we calculated using eq 2 for clusters (iii) and (iv). Using bootstrap resampling statistics,[82,83] we confirmed that the differences among these four mean ΔI values are statistically significant at the α = 0.05 level, and we present confidence intervals

TABLE 1. Average Values of ΔI, Excluded Volumes Λ, Diameters of Spherical A$\beta_{(1\text{-}40)}$ Aggregates θ_S, and Cross-Sectional Areas A_X As Well As Corresponding Cylindrical Diameters θ_C of Rod-Shaped A$\beta_{(1\text{-}40)}$ Aggregates in Each Cluster Compared to Equivalent Values Measured *via* TEM and Values Reported in the Literature

cluster	$\langle\Delta I\rangle$ (min, max), pA	Λ (min, max), nm^3	θ_S (min, max), nm	TEM value,[a] nm	literature value, nm
(i) spherical oligomers	383 (250, 777)	101 (66[b], 205)	5.8 (5.0, 7.3)	$\theta_S = 6.2 \pm 1.2$	$\theta_S = 3-5$ [ref 80]
(ii) protofibrils $I_M \leq I_{eff}$	1177 (787, 1874)	403 (244, 683)		$\theta_C = 6.5 \pm 2.0$	$\theta_C = 5$ [ref 23,25]

cluster	$\langle\Delta I\rangle$, pA	A_X, nm^2	θ_C, nm	TEM value, nm	literature value, nm
(iii) protofibrils $I_M > I_{eff}$	2668 (1953, 3397)	24.5 (18, 31)	5.6 (4.8, 6.3)	$\theta_C = 6.4 \pm 1.5$	$\theta_C = 5$ [ref 23,25]
(iv) fibers $I_M \gg I_{eff}$	4340 (3548, 9552)	40 (33, 88)	7.1 (6.4, 10.6)	$W_1 = 5.6 \pm 0.8$[c]	$W_1 = 6.6$ [ref 26]
				$W_2 = 11.5 \pm 1.5$	$W_2 = 13.2$ [ref 26]
				$A_X \approx 51 \pm 10$ nm^2	$A_X = 30-90$ nm^2 [ref 26,27,31]

[a] Errors shown are standard deviations. [b] Using the average molecular weight density of A$\beta_{(1-40)}$ aggregates of 0.81 kDa/nm^3 [26,81] and the molecular weight of an A$\beta_{(1-40)}$ monomer of 4.355 kDa, the smallest spherical oligomers detected in cluster (i) corresponding to a molecular volume of 250 nm^3, contained approximately 12 Aβ monomers. Completing this same calculation, ΔI values in cluster (i) correspond to aggregates ranging from approximately 12 to 38 monomers, and ΔI values in cluster (ii) correspond to aggregates ranging from 55 to 156 monomers. [c] W_1 and W_2 refer to the widths of twisting A$\beta_{(1-40)}$ fibers when the fibers are twisted or crossing over themselves, W_1, or when the fibers are lying flat, W_2, on the TEM grid (Figure 3).[26] Values in brackets correspond to the minimum and maximum values.

for the mean values in Supporting Information S4. Table 1 also compares the sizes of A$\beta_{(1-40)}$ aggregates determined by resistive-pulse analysis with those determined by TEM from the same samples (Figure 3) as well as with literature values. For instance, the mean ΔI value of the resistive pulses in cluster (i) corresponds to a spherical diameter of 5.8 nm (with a range of 5−7.3 nm), and we measured by TEM that the smallest spherical aggregates had an average diameter of 6.2 ± 1.2 nm (N = 18) (Figure 3A). Similarly, the mean ΔI value of the resistive pulses in cluster (iii) due to protofibrils with $I_M > I_{eff}$ corresponds to a cylindrical diameter of 5.6 nm (with a range of 4.8 to 6.3 nm). In TEM micrographs, we observed protofibrils with an average diameter of 6.4 ± 1.5 nm (N = 117) and with lengths ranging from ∼6 to 350 nm (Figure 3B and C); the reported diameter of protofibrils in the literature is ∼5 nm.[23,25] Finally, the mean ΔI value of resistive pulses in cluster (iv) due to fibers corresponds to a cross-sectional area of 40 nm^2 (with a range of 33 to 88 nm^2). From the TEM micrographs, we estimated the cross-sectional area of A$\beta_{(1-40)}$ fibers to be 51 ± 10 nm^2 (N = 27) based on the two visible widths of the twisting fibers of 5.6 ± 0.8 and 11.5 ± 1.5 nm (Figure 3A: Day 3 and Figure 3D). The literature values of the cross-sectional areas of amyloid fibers range from 30 to 90 nm^2.[2,26,27,31] For these three forms of A$\beta_{(1-40)}$ aggregates, the general agreement among the sizes determined from resistive-pulse analysis with those determined by TEM analysis and those reported in the literature demonstrates that resistive-pulse analysis makes it possible to characterize Aβ oligomers, protofibrils, and fibers in solution. This agreement also indicates that the cluster analysis in Figure 2 produced reasonable assignments for the majority of the resistive pulses. For instance, on the basis of values from TEM analysis, the ratio between the cross-sectional area of fibrils and protofibrils is 1.58 ± 0.8.[84] According to eq 2, we expect the ratio between the mean ΔI value from the translocation of Aβ fibrils in cluster (iv) and the mean ΔI value from the translocation of Aβ protofibrils in cluster (iii) to have this same value, if the cluster assignment was accurate and if the Aβ aggregates in clusters (iii) and (iv) were longer than the length of the pore. Indeed, the ratio of the mean ΔI values between clusters (iv) and (iii) was 1.63 ± 0.3 and not statistically different from the expected value of 1.58. We discuss additional evidence for the accuracy of the cluster analysis in the Supporting Information Section S3 and provide results from the bootstrap resampling statistics in Supporting Information S4.

In order to estimate the excluded volume, Λ, of the protofibrils with $I_M < I_{eff}$ from the resistive pulses in cluster (ii), we made two assumptions. First, protofibrils pass through the nanopore with their long axis aligned parallel to the electric field, resulting in a relatively constant shape factor that can be approximated from the shape factor of a prolate aligned parallel to an electric field, $\gamma_{\|}$. This alignment is predicted because aggregates approaching the nanopore from the bulk solution experience a strong converging electric field gradient.[55,75−77,85−87] Ai and Qian recently modeled the dynamics of nanorods (1 nm × 10 nm) approaching a nanopore under similar conditions to those reported here and demonstrated that rods will completely align with their length axis parallel to the electric field prior to entering the nanopore.[88] Furthermore, the distribution of translocation times in cluster (ii) was narrower than the distribution in cluster (i) (Figure 2B). This result suggests reduced diffusive spreading due to accelerated motion through the pore as a result of reduced viscous drag on aggregates in cluster (ii) compared to those in cluster (i) (see Supporting Information S6 for distributions of t_d values in clusters i and ii).[67,70] Indeed, prolate spheroids moving parallel to their long axis experience less viscous drag than a spherical particle of similar volume.[89] These effects combined with the strong electrophoretic force on an Aβ aggregate due to the net negative charge of each monomer of approximately −3 at pH 7.0[19,90] and the

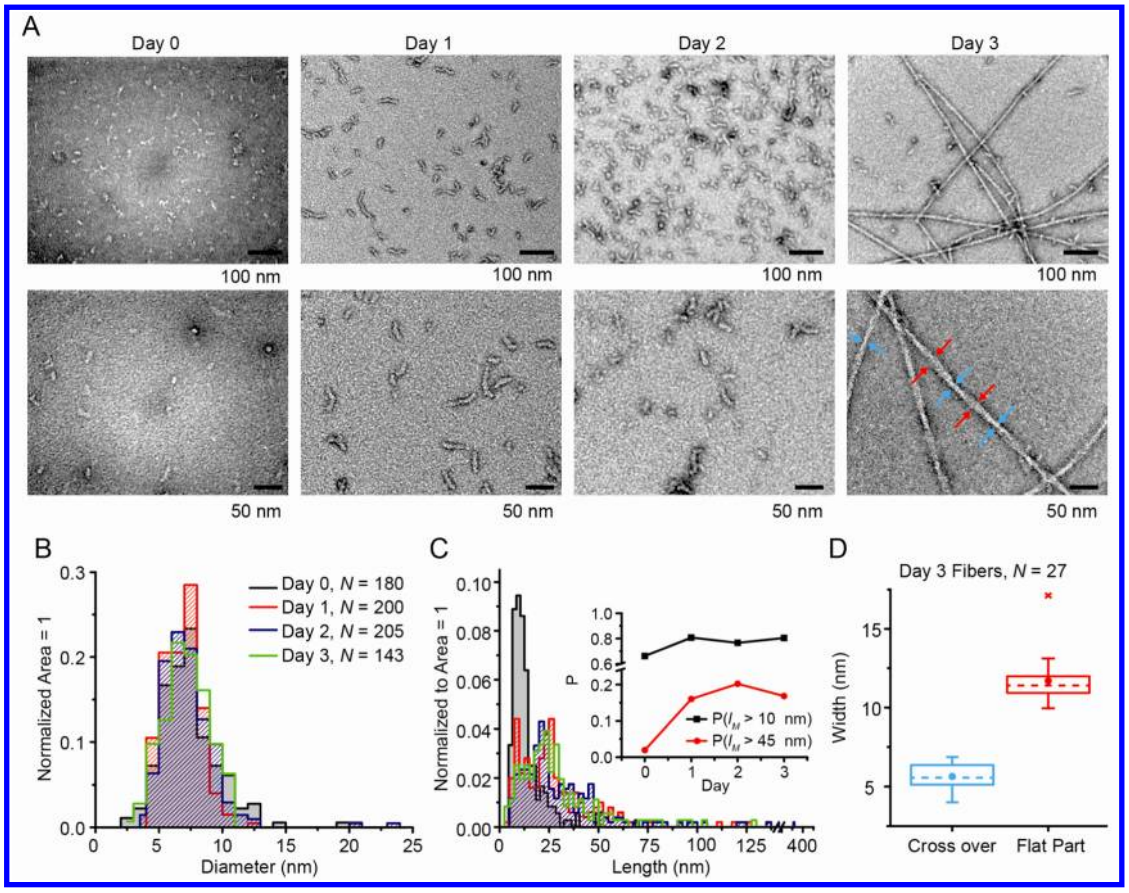

Figure 3. Transmission electron microscopy (TEM) analysis of the size of A$\beta_{(1-40)}$ aggregates. (A) Micrographs showing aggregates with increasing size after incubation in water for 0, 1, 2, and 3 days. Histograms of the diameters (B) and lengths (C) of all aggregates that were not mature fibers. Inset in C: Proportion of aggregates with lengths longer than 10 and 45 nm. (D) Box plots characterizing mature fibers after 3 days of aggregation. The fibers were characterized by their apparent widths when lying flat, W_2 (red arrows in A), on the TEM grid and when twisted or crossing over themselves, W_1 (blue arrows in A), on the TEM grid.[26] The box represents the range between the 1st and 3rd quartiles, the dashed line represents the median, the dot is the mean, and the whiskers extend to the range of the data (minimum and maximum values) except for one outlier, which is plotted as "×".

high electric field in the nanopore ($V_A/l_{eff} = 4.5 \times 10^6\,V\,m^{-1}$) likely orient protofibril aggregates with their long axis parallel to the electric field in the nanopore. The second assumption, based on results by Kellermayer *et al.*, was that the elongation of Aβ protofibrils occurs at a constant average diameter, θ_C, for lengths greater than 6.5 nm.[12] We confirmed the validity of this assumption by TEM analysis of the samples used here (see Figure 3 and Supporting Information S7). Consequently, the excluded volume of these protofibrils could be described by the equation of a cylinder, $\Lambda = 1/4\,\pi\,\theta_C^2 l_M$, and calculated by solving a system of equations that includes the shape factor $\gamma_{||}$ as a function of the length of the aggregate, l_M, and ΔI as a function of $\gamma_{||}$ and l_M. We summarized the details of these equations, the resulting shape factors, and results of this analysis in the Supporting Information S8. Solving this system of equations while using the values of ΔI from the resistive pulses in cluster (ii) and the average diameter of protofibrils (θ_C = 5.6 nm, Table 1), this analysis returned shape factors for each translocation event that ranged from $\gamma_{||}$ = 1.06 to 1.25 (average $\gamma_{||}$ = 1.15) and excluded volumes that ranged from 244 to 683 nm^3 (Table 1).

As a first attempt at examining the peaks in the distribution of A$\beta_{(1-40)}$ sizes reported by Cabriolu *et al.*, we determined the lengths of the protofibrils in clusters (i) and (ii) by using the equations described in Supporting Information S8. From the resulting data, we generated an empirical cumulative distribution (Figure 4 inset) of protofibril lengths in these two clusters.[91] In order to test if this cumulative distribution of protofibril lengths was multimodal, we fit it with a trimodal Gaussian cumulative distribution function (trimodal CDF) and confirmed *via* a Kolmogorov–Smirnov test that the differences between the two distributions were not statistically significant ($p = 0.28$). This result indicates that the trimodal CDF described the empirical distribution very well. In contrast, differences between the empirical cumulative distributions and best curve fits to CDFs for the normal, log-normal, extreme value, exponential, or Poisson distributions were all statistically significant ($p = 0$, $p = 3.2 \times 10^{-8}$, $p = 0.001$, $p = 0.0007$, $p = 2 \times 10^{-27}$, respectively), indicating that these unimodal distributions did not fit the data well.

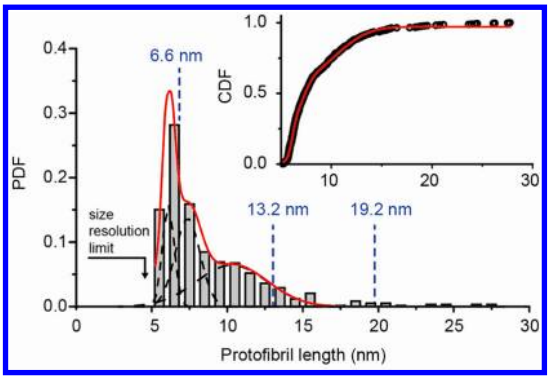

Figure 4. Distributions of estimated lengths of A$\beta_{(1-40)}$ protofibrils in clusters (i) and (ii). The blue dotted lines indicate the location of local maxima in the size distributions of A$\beta_{(1-40)}$ predicted by Cabriolu *et al.*[11] The trimodal Gaussian distribution was obtained by fitting the empirical cumulative distribution shown as black symbols in the inset followed by differentiating the best-curve fit to this cumulative distribution. Inset: Empirical cumulative distribution of protofibril lengths (black points) and fit with a trimodal Gaussian cumulative distribution function (red curve). Bootstrap resampling and refitting procedures revealed that the mean and 95% confidence interval for the means of each peak in the PDF were located at lengths of 6.1 (6.06–6.13) nm, 7.4 (7.22–7.51) nm, and 10.3 (10.16–10.40) nm.

To test the robustness of the analysis of the data in Figure 4, we used bootstrap resampling followed by *k-means* clustering and protofibril length estimation. In each resampling iteration, we generated an empirical cumulative distribution and fit it with the trimodal CDF. In each case the fitting procedure returned similar values for the three modes of the distributions as well as the standard deviations (Figure 4, caption).

For comparison, the dotted blue lines in Figure 4 indicate the lengths of protofibrils at which Cabriolu *et al.* predicted peaks in the distribution of sizes; these lengths are 6.6, 13.2, and 19.2 nm.[11] Kellermayer *et al.* reported segmented growth of Aβ protofibrils generated by the 25–35 amino acid portion of A$\beta_{(1-40)}$ that led to protofibril lengths of 6.5, 13.3, 23.2, 32.5, and 40 nm.[12,92] These reports, together with the observation of multimodal distribution in Figure 4, suggest that protofibrils of A$\beta_{(1-40)}$ occur in solution with certain preferred lengths corresponding to local minima in the work for fibril formation as reported by Cabriolu *et al.* and Kellermayer *et al.* In the work presented here, these lengths correspond to oligomers composed of the following numbers of monomers: 28, 34, and 47.

Since nanopore-based resistive-pulse sensing detects single aggregates, the frequency of translocation events is proportional to the concentration of the aggregates in solution.[73,93–95] Therefore, monitoring the frequency and magnitude of resistive pulses due to Aβ aggregates has the potential to reveal information on the kinetics of aggregation. The frequency of events is, however, also a function of aggregate diffusion to the pore and, hence, the size and shape of the aggregates. Consequently, a direct comparison between frequencies observed in different clusters is not possible. For instance, for identical

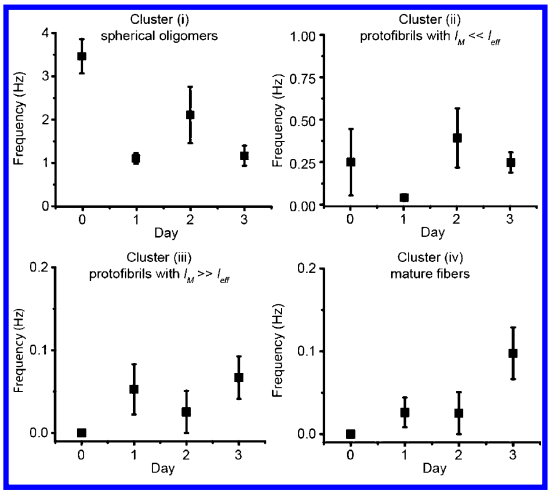

Figure 5. Frequency of translocation events organized by cluster classification reveals time-dependent aggregation. Mean values and standard deviations were calculated by counting the number of translocation events within a given cluster classification during several recordings totaling 40–100 s in duration.

concentrations of Aβ fibers and small Aβ oligomers, the frequency of fiber translocations would be significantly lower than the frequency of oligomer translocations due to the reduced diffusion constant of large fibers compared to oligomers. Additionally, for long protofibrils and fibers, the frequency of events may be affected by steric and entropic effects that influence "threading" of these rod-like species into the nanopore.[70,96,97] With these limitations in mind, Figure 5 shows the frequency of translocation events as a function of the aggregation time within each cluster separately. Assuming that the diffusion constant and barriers to entering the nanopore are similar for all aggregates within a cluster, these four plots provide an indication of the changes in the concentration of aggregates in each cluster. For instance, Figure 5 reveals that the frequency of events due to the translocation of large, mature fibers in cluster (iv) increased over three days, while the frequency of events due to small spherical oligomers in cluster (i) decreased as expected for time-dependent aggregation of Aβ.[98] Figure 5 also shows that the frequency of translocation events of short protofibrils in cluster (ii) remained relatively constant within the error of the measurement. This result is consistent with an intermediate species in a nucleation-dependent process that has reached a steady-state concentration. Combined with the decreasing frequencies observed in cluster (i) and with the increasing frequencies observed in clusters (iii) and (iv), it suggests that the number of aggregates growing large enough to move into cluster (ii) from cluster (i) was approximately equal to the number of aggregates growing large enough to move from cluster (ii) into cluster (iii) during the three-day aggregation process examined in this work.

CONCLUSIONS

We report the use of nanopores with fluid walls for detecting and characterizing size distributions of

unlabeled aggregates of $A\beta_{(1-40)}$ *in situ*. These distributions were obtained by measuring hundreds of single aggregates, making it possible to characterize the large range of Aβ aggregate sizes and shapes. The results from this analysis agree well with those from TEM analysis of the same Aβ preparations and with literature values. Several challenges remain, however, including accurately applying the shape factor, γ, to estimate the distribution of protofibril lengths in clusters (i) and (ii). To improve this analysis, it would be helpful to account for possible rotation of short protofibrils with a low aspect ratio while they move through the confining pore as well as the corresponding electric field lines around the molecule.[78] Another challenge involves the time and size resolution of the technique; currently, Aβ aggregates smaller than dodecamers could not be included in the analysis due to resolution limits in ΔI values and t_d values. Reducing the translocation speed of $A\beta_{(1-40)}$ aggregates should improve the determination of ΔI values, reduce the ΔI threshold, and ensure that all t_d values can be determined accurately. Inclusion of lipids in the bilayer coating that preferentially interact with aggregated forms of Aβ such as phosphatidylserine[99] or the ganglioside GM1[100,101] may be one strategy. Another challenge is that the high ionic strength of the recording electrolyte accelerates the aggregation of Aβ (see Supporting Information S2 and S9). Nanopores with smaller dimensions than the pore used here combined with techniques to increase translocation times may ultimately enable the use of electrolyte solutions with physiologic ionic strength in these assays.

Despite these challenges, we show that nanopore-based resistive-pulse recordings made it possible to characterize the size and shape of unlabeled aggregates of disease-relevant amyloids in solution. The particular strength of nanopore sensing lies in its ability to characterize a large number of individual aggregates. This capability for single-particle analysis is required to characterize Aβ aggregates with a wide-ranging, dynamic heterogeneity in size and shape as well as to correlate cytotoxicity and pathogenic mechanisms with aggregate sizes and shapes.[10]

EXPERIMENTAL SECTION

Preparation of Aβ Aggregates. We received $A\beta_{(1-40)}$ peptides in powder form from GL Biochem Ltd. (Shanghai) with a purity above 98% as determined by HPLC. To remove aggregates of $A\beta_{(1-40)}$ and solubilize $A\beta_{(1-40)}$ in predominantly monomeric form (see Supporting Information, Figure S3), we dissolved the powder in hexafluoroisopropanol (HFIP) to a concentration of 1 mM of $A\beta_{(1-40)}$.[28] After 24 h incubation in HFIP, we diluted this solution with cold (4 °C) deionized water at a 2:1 (v/v) ratio (H_2O:HFIP). We then rapidly aliquoted the solution, immediately froze it in a liquid nitrogen bath, and lyophilized the frozen aliquots for two days. This procedure removes HFIP to amounts that are below detectable levels of fluorine-NMR (Supporting Information S2). To start the aggregation process of $A\beta_{(1-40)}$ peptides, we dissolved the lyophilized powder in deionized water to a concentration of 1 mg $\times$ mL^{-1}. We incubated these samples in 0.5 mL closed siliconized plastic microcentrifuge tubes (Fisherbrand low-retention siliconized tubes) on a temperature-controlled shaker (Thermomixer, Eppendorf) set to 750 rpm at a temperature of 22 °C for zero, one, two, and three days.

Nanopore-Based Sensing Experiments. To detect aggregates of $A\beta_{(1-40)}$, we first formed a supported lipid bilayer of 1-palmitoyl-2-oleoyl-*sn*-glycero-3-phosphocholine lipids (Avanti Polar Lipids, Inc.) on a nanopore that was 28 nm in diameter and had a length of 18 nm, resulting in a coated diameter of approximately 18 nm and coated length of 28 nm.[39] We described details of the bilayer formation in Yusko *et al.*[39] We added solutions containing $A\beta_{(1-40)}$ to the top solution compartment of the fluidic setup (2 M KCl with 10 mM HEPES pH 7.4) such that the final concentration of $A\beta_{(1-40)}$ ranged from 0.007 to 0.025 mg $\times$ mL^{-1}. We recorded resistive pulses at an applied potential difference of -0.2 V with the polarity referring to the top fluid compartment relative to the bottom fluid compartment, which was connected to a ground. Recordings were completed within 10 to 15 min of adding $A\beta_{(1-40)}$.

We used Ag/AgCl pellet electrodes (Warner Instruments) to monitor ionic currents through electrolyte-filled nanopores with a patch-clamp amplifier (Axopatch 200B, Molecular Devices Inc.) in voltage-clamp mode (*i.e.*, at constant applied voltage). We set the analog low-pass filter of the amplifier to a cutoff frequency of 100 kHz. We used a digitizer (Digidata 1322) with a sampling frequency of 500 kHz in combination with a program written in LabView to acquire and store data.[102] To distinguish resistive pulses reliably from the electrical noise, we first filtered the data digitally with a Gaussian low-pass filter (f_c =15 kHz) in MATLAB and then used a modified form of the custom written MATLAB routine described in Pedone *et al.*[63] We modified the MATLAB routine to calculate the translocation time, t_d, as the width of individual resistive pulses at half of their peak amplitude, also known as the full-width-half-maximum value.[39,70] From this analysis we obtained the ΔI and t_d values for each resistive pulse.

Preparation of Transmission Electron Microcopy Samples. We prepared samples for transmission electron microscopy (TEM) analysis using a negative staining method and glow-discharged, carbon-coated copper grids (Electron Microscopy Sciences, cat no. FCF-200-Cu). We applied 5 μL of each Aβ sample (1 mg $\times$ mL^{-1}), which had been permitted to aggregate in pure water for zero, one, two, or three days, to the glow-discharged carbon-coated copper grid. After 2 min, we wicked the fluid off the grids with filter paper and washed the grids with a 5 μL drop of deionized water for 1 min. After wicking off the fluid again, we applied a 5 μL drop of 2% uranyl acetate for 1 min, wicked off the excess fluid on the grids, and allowed the grids to dry.

Conflict of Interest: The authors declare no competing financial interest.

Acknowledgment. The authors thank D. Pedone and the group of U. Rant for the MATLAB routines used to analyze current recordings. The authors also thank D. J. Estes and J. D. Uram for their work on the LabView recording software. This work was supported by a National Science Foundation Career Award (M.M., grant no. 0449088), the National Institutes of Health (M.M., grant no. 1R01GM081705), and the National Human Genome Research Institute (J.L., grant nos. HG003290 and HG004776). E.C.Y. acknowledges a Graduate Assistance in Areas of National Need Fellowship. P.P. acknowledges a fellowship from the government of Thailand. The TEM work was performed in the Electron Microbeam Analysis Laboratory at the University of Michigan under NSF grant no. 0315633.

Supporting Information Available: Detailed descriptions of control experiments, preparation of Aβ aggregates, toxicity of Aβ preparations, bootstrap resampling statistics, distributions

of t_d values, equations to estimate the length of protofibrils from ΔI values, and additional TEM micrographs and characterization are provided. This material is available free of charge *via* the Internet at http://pubs.acs.org.

REFERENCES AND NOTES

1. Trojanowski, J. Q.; Mattson, M. P. Overview of Protein Aggregation in Single, Double, and Triple Neurodegenerative Brain Amyloidoses. *Neuromol. Med.* **2003**, *4*, 1–5.
2. Morgado, I.; Fandrich, M. Assembly of Alzheimer's A-Beta Peptide into Nanostructured Amyloid Fibrils. *Curr. Opin. Colloid Interface Sci.* **2011**, *16*, 508–514.
3. Querfurth, H. W.; LaFerla, F. M. Mechanisms of Disease Alzheimer's Disease. *N. Engl. J. Med.* **2010**, *362*, 329–344.
4. Selkoe, D. J. Clearing the Brain's Amyloid Cobwebs. *Neuron* **2001**, *32*, 177–180.
5. Selkoe, D. J. Resolving Controversies on the Path to Alzheimer's Therapeutics. *Nat. Med.* **2011**, *17*, 1060–1065.
6. Hardy, J. A Hundred Years of Alzheimer's Disease Research. *Neuron* **2006**, *52*, 3–13.
7. Schnabel, J. Little Proteins, Big Clues. *Nature* **2011**, *475*, S12–S14.
8. Ding, H.; Wong, P. T.; Lee, E. L.; Gafni, A.; Steel, D. G. Determination of the Oligomer Size of Amyloidogenic Protein Beta-Amyloid(1−40) by Single-Molecule Spectroscopy. *Biophys. J.* **2009**, *97*, 912–921.
9. Johnson, R. D.; Schauerte, J. A.; Wisser, K. C.; Gafni, A.; Steel, D. G. Direct Observation of Single Amyloid-Beta-(1−40) Oligomers on Live Cells: Binding and Growth at Physiological Concentrations. *PLoS One* **2011**, *6*.
10. Ono, K.; Condron, M. M.; Teplow, D. B. Structure-Neurotoxicity Relationships of Amyloid Beta-Protein Oligomers. *Proc. Natl. Acad. Sci. U. S. A.* **2009**, *106*, 14745–14750.
11. Cabriolu, R.; Kashchiev, D.; Auer, S. Size Distribution of Amyloid Nanofibrils. *Biophys. J.* **2011**, *101*, 2232–2241.
12. Kellermayer, M. S. Z.; Karsai, Á.; Benke, M.; Soós, K.; Penke, B. Stepwise Dynamics of Epitaxially Growing Single Amyloid Fibrils. *Proc. Natl. Acad. Sci. U. S. A.* **2008**, *105*, 141–144.
13. Goldsbury, C. S.; Wirtz, S.; Müller, S. A.; Sunderji, S.; Wicki, P.; Aebi, U.; Frey, P. Studies on the *In Vitro* Assembly of Aβ 1−40: Implications for the Search for Aβ Fibril Formation Inhibitors. *J. Struct. Biol.* **2000**, *130*, 217–231.
14. Lines, R. W. The Electrical Sensing Zone Method (the Coulter Principle). In *Particle Size Analysis*, Stanley-Wood, N. G.; Lines, R. W., Eds.; The Royal Society of Chemistry: Cambridge, 1992; p 352.
15. Demuro, A.; Mina, E.; Kayed, R.; Milton, S. C.; Parker, I.; Glabe, C. G. Calcium Dysregulation and Membrane Disruption as a Ubiquitous Neurotoxic Mechanism of Soluble Amyloid Oligomers. *J. Biol. Chem.* **2005**, *280*, 17294–17300.
16. Giuffrida, M. L.; Caraci, F.; Pignataro, B.; Cataldo, S.; De Bona, P.; Bruno, V.; Molinaro, G.; Pappalardo, G.; Messina, A.; Palmigiano, A.; *et al*. Beta-Amyloid Monomers are Neuroprotective. *J. Neurosci.* **2009**, *29*, 10582–10587.
17. Hartley, D. M.; Walsh, D. M.; Ye, C. P. P.; Diehl, T.; Vasquez, S.; Vassilev, P. M.; Teplow, D. B.; Selkoe, D. J. Protofibrillar Intermediates of Amyloid Beta-Protein Induce Acute Electrophysiological Changes and Progressive Neurotoxicity in Cortical Neurons. *J. Neurosci.* **1999**, *19*, 8876–8884.
18. Bucciantini, M.; Giannoni, E.; Chiti, F.; Baroni, F.; Formigli, L.; Zurdo, J. S.; Taddei, N.; Ramponi, G.; Dobson, C. M.; Stefani, M. Inherent Toxicity of Aggregates Implies a Common Mechanism for Protein Misfolding Diseases. *Nature* **2002**, *416*, 507–511.
19. Hortschansky, P.; Schroeckh, V.; Christopeit, T.; Zandomeneghi, G.; Fandrich, M. The Aggregation Kinetics of Alzheimer's Beta-Amyloid Peptide is Controlled by Stochastic Nucleation. *Protein Sci.* **2005**, *14*, 1753–1759.
20. Zagorski, M. G.; Shao, H.; Ma, K.; Li, H.; Yang, J.; Zeng, H. Amyloid Abeta-the Peptide from Hell. *Regul. Pept.* **2001**, *97*, 31.
21. Zagorski, M. G.; Yang, J.; Shao, H. Y.; Ma, K.; Zeng, H.; Hong, A. Methodological and Chemical Factors Affecting Amyloid Beta Peptide Amyloidogenicity. *Methods Enzymol.* **1999**, *309*, 189–204.
22. Parihar, M. S.; Hemnani, T. Alzheimer's Disease Pathogenesis and Therapeutic Interventions. *J. Clin. Neurosci.* **2004**, *11*, 456–467.
23. Walsh, D. M.; Hartley, D. M.; Kusumoto, Y.; Fezoui, Y.; Condron, M. M.; Lomakin, A.; Benedek, G. B.; Selkoe, D. J.; Teplow, D. B. Amyloid Beta-Protein Fibrillogenesis−Structure and Biological Activity of Protofibrillar Intermediates. *J. Biol. Chem.* **1999**, *274*, 25945–25952.
24. Jan, A.; Hartley, D. M.; Lashuel, H. A. Preparation and Characterization of Toxic A-Beta Aggregates for Structural and Functional Studies in Alzheimer's Disease Research. *Nat. Protoc.* **2010**, *5*, 1186–1209.
25. Roychaudhuri, R.; Yang, M.; Hoshi, M. M.; Teplow, D. B. Amyloid Beta-Protein Assembly and Alzheimer Disease. *J. Biol. Chem.* **2009**, *284*, 4749–4753.
26. Schmidt, M.; Sachse, C.; Richter, W.; Xu, C.; Fandrich, M.; Grigorieff, N. Comparison of Alzheimer A-Beta(1−40) and A-Beta(1−42) Amyloid Fibrils Reveals Similar Protofilament Structures. *Proc. Natl. Acad. Sci. U. S. A.* **2009**, *106*, 19813–19818.
27. Sachse, C.; Fandrich, M.; Grigorieff, N. Paired Beta-Sheet Structure of an A-Beta(1−40) Amyloid Fibril Revealed by Electron Microscopy. *Proc. Natl. Acad. Sci. U. S. A.* **2008**, *105*, 7462–7466.
28. Capone, R.; Quiroz, F. G.; Prangkio, P.; Saluja, I.; Sauer, A. M.; Bautista, M. R.; Turner, R. S.; Yang, J.; Mayer, M. Amyloid-Beta-Induced Ion Flux in Artificial Lipid Bilayers and Neuronal Cells: Resolving a Controversy. *Neurotox. Res.* **2009**, *16*, 1–13.
29. Bitan, G.; Fradinger, E. A.; Spring, S. M.; Teplow, D. B. Neurotoxic Protein Oligomers−What You See Is Not Always What You Get. *Amyloid-J. Protein Fold. Disord.* **2005**, *12*, 88–95.
30. Adamcik, J.; Jung, J. M.; Flakowski, J.; De Los Rios, P.; Dietler, G.; Mezzenga, R. Understanding Amyloid Aggregation by Statistical Analysis of Atomic Force Microscopy Images. *Nat. Nanotechnol.* **2010**, *5*, 423–428.
31. Meinhardt, J.; Sachse, C.; Hortschansky, P.; Grigorieff, N.; Fandrich, M. A Beta(1−40) Fibril Polymorphism Implies Diverse Interaction Patterns in Amyloid Fibrils. *J. Mol. Biol.* **2009**, *386*, 869–877.
32. Kremer, J. J.; Pallitto, M. M.; Sklansky, D. J.; Murphy, R. M. Correlation of Beta-Amyloid Aggregate Size and Hydrophobicity with Decreased Bilayer Fluidity of Model Membranes. *Biochemistry* **2000**, *39*, 10309–10318.
33. Chou, I. H.; Benford, M.; Beier, H. T.; Coté, G. L.; Wang, M.; Jing, N.; Kameoka, J.; Good, T. A. Nanofluidic Biosensing for B-Amyloid Detection Using Surface Enhanced Raman Spectroscopy. *Nano Lett.* **2008**, *8*, 1729–1735.
34. Knowles, T. P. J.; White, D. A.; Abate, A. R.; Agresti, J. J.; Cohen, S. I. A.; Sperling, R. A.; De Genst, E. J.; Dobson, C. M.; Weitz, D. A. Observation of Spatial Propagation of Amyloid Assembly from Single Nuclei. *Proc. Natl. Acad. Sci. U. S. A.* **2011**, *108*, 14746–14751.
35. Schierle, G. S. K.; van de Linde, S.; Erdelyi, M.; Esbjorner, E. K.; Klein, T.; Rees, E.; Bertoncini, C. W.; Dobson, C. M.; Sauer, M.; Kaminski, C. F. *In Situ* Measurements of the Formation and Morphology of Intracellular Beta-Amyloid Fibrils by Super-Resolution Fluorescence Imaging. *J. Am. Chem. Soc.* **2011**, *133*, 12902–12905.
36. Wang, H. Y.; Ying, Y. L.; Li, Y.; Kraatz, H. B.; Long, Y. T. Nanopore Analysis of Beta-Amyloid Peptide Aggregation Transition Induced by Small Molecules. *Anal. Chem.* **2011**, *83*, 1746–1752.
37. Dukes, K. D.; Rodenberg, C. F.; Lammi, R. K. Monitoring the Earliest Amyloid-Beta Oligomers *via* Quantized Photobleaching of Dye-Labeled Peptides. *Anal. Biochem.* **2008**, *382*, 29–34.

38. Schauerte, J. A.; Wong, P. T.; Wisser, K. C.; Ding, H.; Steel, D. G.; Gafni, A. Simultaneous Single-Molecule Fluorescence and Conductivity Studies Reveal Distinct Classes of A-Beta Species on Lipid Bilayers. *Biochemistry* **2010**, *49*, 3031–3039.
39. Yusko, E. C.; Johnson, J. M.; Majd, S.; Prangkio, P.; Rollings, R. C.; Li, J.; Yang, J.; Mayer, M. Controlling Protein Translocation through Nanopores with Bio-Inspired Fluid Walls. *Nat. Nanotechnol.* **2011**, *6*, 253–260.
40. Actis, P.; Rogers, A.; Nivala, J.; Vilozny, B.; Seger, R. A.; Jejelowo, O.; Pourmand, N. Reversible Thrombin Detection by Aptamer Functionalized Sting Sensors. *Biosens. Bioelectron.* **2011**, *26*, 4503–4507.
41. Coulter, W. H. Means for Counting Particles Suspended in a Fluid. U.S. Patent 2,656,508, October 20, 1953.
42. Dekker, C. Solid-State Nanopores. *Nat. Nanotechnol.* **2007**, *2*, 209–215.
43. Kowalczyk, S. W.; Blosser, T. R.; Dekker, C. Biomimetic Nanopores: Learning from and about Nature. *Trends Biotechnol.* **2011**, *29*, 607–614.
44. Howorka, S.; Siwy, Z. Nanopore Analytics: Sensing of Single Molecules. *Chem. Soc. Rev.* **2009**, *38*, 2360–2384.
45. Majd, S.; Yusko, E. C.; Billeh, Y. N.; Macrae, M. X.; Yang, J.; Mayer, M. Applications of Biological Pores in Nanomedicine, Sensing, and Nanoelectronics. *Curr. Opin. Biotechnol.* **2010**, *21*, 439–476.
46. Yusko, E. C.; Billeh, Y. N.; Yang, J.; Mayer, M. Nanopore Recordings to Quanitify Activity-Related Properties of Proteins. In *Nanopores: Sensing and Fundamental Biological Interactions*, Iqbal, S. M.; Bashir, R., Eds.; Springer Publishing Co.: New York, 2011; pp 203−225.
47. Stanley-Wood, N. G.; Lines, R. W. *Particle Size Analysis*; The Royal Society of Chemistry: Cambridge, 1992; p 352.
48. Branton, D.; Deamer, D. W.; Marziali, A.; Bayley, H.; Benner, S. A.; Butler, T.; Di Ventra, M.; Garaj, S.; Hibbs, A.; Huang, X. H.; *et al*. The Potential and Challenges of Nanopore Sequencing. *Nat. Biotechnol.* **2008**, *26*, 1146–1153.
49. Keyser, U. F. Controlling Molecular Transport through Nanopores. *J. R. Soc. Interface* **2011**, *8*, 1369–1378.
50. Ivanov, A. P.; Instuli, E.; McGilvery, C. M.; Baldwin, G.; McComb, D. W.; Albrecht, T.; Edel, J. B. DNA Tunneling Detector Embedded in a Nanopore. *Nano Lett.* **2011**, *11*, 279–285.
51. Iqbal, S. M.; Bashir, R. *Nanoelectronic-Based Detection for Biology and Medicine*; Springer-Verlag: Berlin, 2009; pp 1433−1449.
52. Actis, P.; Jejelowo, O.; Pourmand, N. Ultrasensitive Mycotoxin Detection by Sting Sensors. *Biosens. Bioelectron.* **2010**, *26*, 333–337.
53. Grover, N. B.; Naaman, J.; Ben-sasson, S.; Doljansk, F. Electrical Sizing of Particles in Suspensions. I. Theory. *Biophys. J.* **1969**, *9*, 1398–1414.
54. Grover, N. B.; Naaman, J.; Ben-sasson, S.; Doljansk, F.; Nadav, E. Electrical Sizing of Particles in Suspensions. 2. Experiments with Rigid Spheres. *Biophys. J.* **1969**, *9*, 1415–1425.
55. Solomentsev, Y.; Anderson, J. L. Electrophoresis of Slender Particles. *J. Fluid Mech.* **1994**, *279*, 197–215.
56. Han, A. P.; Creus, M.; Schurmann, G.; Linder, V.; Ward, T. R.; de Rooij, N. F.; Staufer, U. Label-Free Detection of Single Protein Molecules and Protein-Protein Interactions Using Synthetic Nanopores. *Anal. Chem.* **2008**, *80*, 4651–4658.
57. Sexton, L. T.; Mukaibo, H.; Katira, P.; Hess, H.; Sherrill, S. A.; Horne, L. P.; Martin, C. R. An Adsorption-Based Model for Pulse Duration in Resistive-Pulse Protein Sensing. *J. Am. Chem. Soc.* **2010**, *132*, 6755–6763.
58. Cai, Q.; Ledden, B.; Krueger, E.; Golovchenko, J. A.; Li, J. L. Nanopore Sculpting with Noble Gas Ions. *J. Appl. Phys.* **2006**, *100*, 024914.
59. Li, J.; Stein, D.; McMullan, C.; Branton, D.; Aziz, M. J.; Golovchenko, J. A. Ion-Beam Sculpting at Nanometre Length Scales. *Nature* **2001**, *412*, 166–169.
60. Prangkio, P. Investigation of Cytotoxicity and Ion Flux Induced by Various Aggregation States of Amyloid-Beta Peptides. Ph.D. Thesis. University of Michigan: Ann Arbor, MI, August 9, 2011.
61. Horiuchi, M.; Maezawa, I.; Itoh, A.; Wakayama, K.; Jin, L. W.; Itoh, T.; DeCarli, C. Amyloid Beta 1−42 Oligomer Inhibits Myelin Sheet Formation *in Vitro*. *Neurobiol. Aging* **2012**, *33*, 499–509.
62. Brining, S. K. Predicting the *in Vitro* Toxicity of Synthetic Beta-Amyloid (1−40). *Neurobiol. Aging* **1997**, *18*, 581–589.
63. Pedone, D.; Firnkes, M.; Rant, U. Data Analysis of Translocation Events in Nanopore Experiments. *Anal. Chem.* **2009**, *81*, 9689–9694.
64. Fologea, D.; Brandin, E.; Uplinger, J.; Branton, D.; Li, J. DNA Conformation and Base Number Simultaneously Determined in a Nanopore. *Electrophoresis* **2007**, *28*, 3186–3192.
65. Storm, A. J.; Storm, C.; Chen, J. H.; Zandbergen, H.; Joanny, J. F.; Dekker, C. Fast DNA Translocation through a Solid-State Nanopore. *Nano Lett.* **2005**, *5*, 1193–1197.
66. Meller, A.; Nivon, L.; Branton, D. Voltage-Driven DNA Translocations through a Nanopore. *Phys. Rev. Lett.* **2001**, *86*, 3435–3438.
67. Li, J. L.; Talaga, D. S. The Distribution of DNA Translocation Times in Solid-State Nanopores. *J. Phys.-Condens. Matter* **2010**, 22.
68. Rousseeuw, P. J.; Kaufman, L. *Finding Groups in Data: An Introduction to Cluster Analysis*; John Wiley & Sons, Inc.: New York, 1990.
69. Kerr, M. K.; Churchill, G. A. Bootstrapping Cluster Analysis: Assessing the Reliability of Conclusions from Microarray Experiments. *Proc. National Acad. Sci.* **2001**, *98*, 8961–8965.
70. Talaga, D. S.; Li, J. L. Single-Molecule Protein Unfolding in Solid State Nanopores. *J. Am. Chem. Soc.* **2009**, *131*, 9287–9297.
71. Ito, T.; Sun, L.; Crooks, R. M. Simultaneous Determination of the Size and Surface Charge of Individual Nanoparticles Using a Carbon Nanotube-Based Coulter Counter. *Anal. Chem.* **2003**, *75*, 2399–2406.
72. Fologea, D.; Ledden, B.; David, S. M.; Li, J. Electrical Characterization of Protein Molecules by a Solid-State Nanopore. *Appl. Phys. Lett.* **2007**, *91*, 053901.
73. Uram, J. D.; Ke, K.; Hunt, A. J.; Mayer, M. Submicrometer Pore-Based Characterization and Quantification of Antibody-Virus Interactions. *Small* **2006**, *2*, 967–972.
74. Uram, J. D.; Ke, K.; Hunt, A. J.; Mayer, M. Label-Free Affinity Assays by Rapid Detection of Immune Complexes in Submicrometer Pores. *Angew. Chem., Int. Ed.* **2006**, *45*, 2281–2285.
75. DeBlois, R. W.; Uzgiris, E. E.; Cluxton, D. H.; Mazzone, H. M. Comparative Measurements of Size and Polydispersity of Several Insect Viruses. *Anal. Biochem.* **1978**, *90*, 273–288.
76. Golibersuch, D. C. Observation of Aspherical Particle Rotation in Poiseuille Flow *via* the Resistance Pulse Technique. Part 2. Application to Fused Sphere Dumbbells. *J. Appl. Phys.* **1973**, *44*, 2580–2584.
77. Golibersuch, D. C. Observation of Aspherical Particle Rotation in Poiseuille Flow *via* the Resistance Pulse Technique. Part 1. Application to Human Erythrocytes. *Biophys. J.* **1973**, *13*, 265–280.
78. Kozak, D.; Anderson, W.; Vogel, R.; Trau, M. Advances in Resistive Pulse Sensors: Devices Bridging the Void between Molecular and Microscopic Detection. *Nano Today* **2011**, *6*, 531–545.
79. Hille, B. *Ion Channels of Excitable Membranes*; Sinauer Associaties, Inc.: Sunderland, 2001; pp 347−349.
80. Lambert, M. P.; Barlow, A. K.; Chromy, B. A.; Edwards, C.; Freed, R.; Liosatos, M.; Morgan, T. E.; Rozovsky, I.; Trommer, B.; Viola, K. L.; *et al*. Diffusible, Nonfibrillar Ligands Derived from Aβ1−42 Are Potent Central Nervous System Neurotoxins. *Proc. Natl. Acad. Sci. U. S. A.* **1998**, *95*, 6448–6453.
81. Matthews, B. W. Solvent Content of Protein Crystals. *J. Mol. Biol.* **1968**, *33*, 491–&.
82. Adler, J. *R in a Nutshell*; O'Reilly Media, Inc.: Sebastopol, CA, 2010; p 333.

83. Whitlock, M. C.; Schluter, D. *The Analysis of Biological Data*; Roberts and Company Publishers: Greenwood Village, CO, 2009; pp 550−557.
84. In this case the error was propagated using standard error of the mean as opposed to standard deviations.
85. Solomentsev, Y.; Anderson, J. L. Electrophoretic Transport of Spheroidal Colloids in Nonhomogeneous Electric Fields. *Ind. Eng. Chem. Res.* **1995**, *34*, 3231–3238.
86. Wanunu, M.; Morrison, W.; Rabin, Y.; Grosberg, A. Y.; Meller, A. Electrostatic Focusing of Unlabelled DNA into Nanoscale Pores Using a Salt Gradient. *Nat. Nanotechnol.* **2010**, *5*, 160–165.
87. Bretherton, F. P. The Motion of Rigid Particles in a Shear Flow at Low Reynolds Number. *J. Fluid Mech.* **1962**, *14*, 284–304.
88. Ai, Y.; Qian, S. Direct Numerical Simulation of Electrokinetic Translocation of a Cylindrical Particle through a Nanopore Using a Poisson-Boltzmann Approach. *Electrophoresis* **2011**, *32*, 996–1005.
89. Berg, H. C. *Random Walks in Biology*; Princeton University Press: Princeton, NJ, 1993.
90. Guo, M.; Gorman, P. M.; Rico, M.; Chakrabartty, A.; Laurents, D. V. Charge Substitution Shows That Repulsive Electrostatic Interactions Impede the Oligomerization of Alzheimer Amyloid Peptides. *FEBS Lett.* **2005**, *579*, 3574–3578.
91. We conducted the analysis based on empirical cumulative distributions because this approach has the advantage that it does not require binning of data. Avoiding binning circumvents problems of selecting adequate bin widths.[39] By fitting a theoretical cumulative distribution function to the empirical cumulative distribution and differentiating it, we generated the probability density function that overlays the histogram in Figure 4.
92. Since the density of observations at 6.1 nm in Figure 4 is extremely high, features of the distribution beyond ∼12−13 nm may be obscured. To overcome this limitation, we explored empirical cumulative distributions generated only from events classified into cluster (ii) (see Supporting Information S8). Best curve fitting to these empirical distribution functions revealed modes at 11, 15.5, 18.8, and 24 nm; however, in this case the empirical distribution was not statistically different from an exponential distribution (Supporting Information S8).
93. An, R.; Uram, J. D.; Yusko, E. C.; Ke, K.; Mayer, M.; Hunt, A. J. Ultrafast Laser Fabrication of Submicrometer Pores in Borosilicate Glass. *Opt. Lett.* **2008**, *33*, 1153–1155.
94. Sun, L.; Crooks, R. M. Single Carbon Nanotube Membranes: A Well-Defined Model for Studying Mass Transport through Nanoporous Materials. *J. Am. Chem. Soc.* **2000**, *122*, 12340–12345.
95. Lee, S.; Zhang, Y. H.; White, H. S.; Harrell, C. C.; Martin, C. R. Electrophoretic Capture and Detection of Nanoparticles at the Opening of a Membrane Pore Using Scanning Electrochemical Microscopy. *Anal. Chem.* **2004**, *76*, 6108–6115.
96. Bikwemu, R.; Wolfe, A. J.; Xing, X. J.; Movileanu, L. Facilitated Translocation of Polypeptides through a Single Nanopore. *J. Phys.-Condens. Matter* **2010**, *22*.
97. Bacri, L.; Oukhaled, A. G.; Schiedt, B.; Patriarche, G.; Bourhis, E.; Gierak, J.; Pelta, J.; Auvray, L. Dynamics of Colloids in Single Solid-State Nanopores. *J. Phys. Chem. B* **2011**, *115*, 2890–2898.
98. Harper, J. D.; Lansbury, P. T. Models of Amyloid Seeding in Alzheimier's Disease and Scrapie: Mechanistic Truths and Physiological Consequences of the Time-Dependent Solubility of Amyloid Proteins. *Annu. Rev. Biochem.* **1997**, *66*, 385–407.
99. Simakova, O.; Arispe, N. J. The Cell-Selective Neurotoxicity of the Alzheimer's A-Beta Peptide is Determined by Surface Phosphatidylserine and Cytosolic ATP Levels. Membrane Binding Is Required for a Beta Toxicity. *J. Neurosci.* **2007**, *27*, 13719–13729.
100. Vestergaard, M.; Hamada, T.; Takagi, M. Using Model Membranes for the Study of Amyloid Beta: Lipid Interactions and Neurotoxicity. *Biotechnol. Bioeng.* **2008**, *99*, 753–763.
101. Williams, T. L.; Serpell, L. C. Membrane and Surface Interactions of Alzheimer's A-Beta Peptide−Insights into the Mechanism of Cytotoxicity. *Febs J.* **2011**, *278*, 3905–3917.
102. Uram, J. D.; Ke, K.; Mayer, M. Noise and Bandwidth of Current Recordings from Submicrometer Pores and Nanopores. *ACS Nano* **2008**, *2*, 857–872.